Layer-Dependent Band Gaps of Platinum-Dichalcogenides

Li, J.; Kolekar, S.; Ghorbani Asl, M.; Lehnert, T.; Biskupek, J.; Kaiser, U.;
Krasheninnikov, A.; Batzill, M.;

Originally published:

August 2021

ACS Nano 15(2021), 13249-13259

DOI: https://doi.org/10.1021/acsnano.1c02971

Layer-Dependent Band Gaps of Platinum-Dichalcogenides

Jingfeng Li,[1] Sadhu Kolekar,[1] Mahdi Ghorbani-Asl,[2] Tibor Lehnert,[3] Johannes Biskupek,[3]
Ute Kaiser,[3] Arkady V. Krasheninnikov,[2,4] Matthias Batzill[1,*]

[1] Department of Physics, University of South Florida, Tampa, FL 33620, USA
[2] Helmholtz-Zentrum Dresden-Rossendorf, Institute of Ion Beam Physics and Materials Research, 01328 Dresden, Germany
[3] Electron Microscopy Group of Materials Science, Ulm University, 89081 Ulm, Germany
[4] Department of Applied Physics, Aalto University, P.O. Box 11100, 00076 Aalto, Finland

[*] Corresponding author: Matthias Batzill; e-mail: mbatzill@usf.edu

TOC-figure:

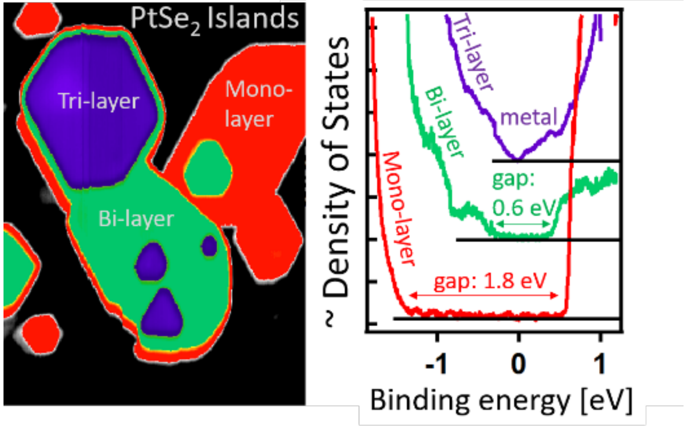

Abstract:

Owing to the relatively strong inter-layer interaction, the platinum-dichalcogenides exhibit tunability of their electronic properties by controlling the number of layers. Both $PtSe_2$ and $PtTe_2$ display a semi-metal to semi-conductor transition as they are reduced to bi- or single-layer. The value of the fundamental band gap, however, has been inferred only from density functional theory (DFT) calculations, which are notoriously challenging, as different methods give different results, and currently there is no experimental data. Here we determine the band gap as a function of the number of layers by local scanning tunneling spectroscopy on MBE-grown $PtSe_2$ and $PtTe_2$ islands. We find band gaps of 1.8 eV and 0.6 eV for mono- and bi-layer $PtSe_2$, respectively, and 0.5 eV for monolayer $PtTe_2$. Tri-layer $PtSe_2$ and bilayer $PtTe_2$ are semi-metallic. The experimental data are compared to DFT calculations carried out at different levels of theory. The calculated band gaps may differ significantly from the experimental values, emphasizing the importance of the experimental work. We further show that the variations in the calculated fundamental band gap in bilayer $PtSe_2$ are related to the computed separation of the layers, which depends on the choice of the van der Waals functional. This sensitivity of the band gap to inter-layer separation also suggests that the gap can be tuned by uniaxial stress and our simulations indicate that only modest pressures are required for a significant reduction of the gap, making Pt-dichalcogenides suitable materials for pressure-sensing.

Keywords: 2D materials; layer dependence; $PtSe_2$; $PtTe_2$; scanning tunneling spectroscopy; van der Waals materials; transition metal dichalcogenides.

Layered transition metal dichalcogenides (TMDs) are a diverse class of materials[1,2,3] whose strong anisotropic structure of in-plane covalent bonding and only weak van der Waals interactions between molecular planes enable the reduction of their dimensions to single molecular layers without breaking covalent bonds. Although no bonds are broken, mono- or few- molecular layer thick TMDs frequently exhibit different properties as compared to their bulk counterpart materials.[4,5,6,7,8,9,10,11,12] Electronic structure may be altered due to a combination of quantum confinement effects and the lack of interlayer interactions of the frontier electronic orbitals between the layers. These interlayer interactions and thus the layer dependent properties vary for different members of the TMD family. Density functional theory (DFT) calculations have suggested that interlayer interactions are particularly strong in the Pt-dichalcogenides.[13,14,15,16,17] While PtS_2 is semiconducting, $PtSe_2$ and $PtTe_2$ are (semi)metallic in their bulk form, with the chalcogen *p*-derived electron pockets at the Γ-point and hole pockets at the K-point. A more detailed Fermi-surface sampling also showed a hole pocket at non-symmetry points in the 3D Brillouin zone (BZ) within the Γ-M-L-A plane for 1T-$PtSe_2$.[18] In bulk materials these Pt-dichalcogenides have attracted significant interest because of its topologically protected bands[19,20,21,22] and defect induced magnetism[23] that may persists down to the mono- and bi-layer thickness.[24] By thinning the material to single molecular sheets, both $PtSe_2$ and $PtTe_2$ exhibits a transition to a semiconducting material with significant band gaps opening for the monolayer. On a DFT-level,[14] band gaps of 1.18 eV have been predicted for monolayer and 0.24 eV for bilayer $PtSe_2$. For $PtTe_2$ a 0.4 eV band gap for monolayer $PtTe_2$ has been predicted, while bilayer $PtTe_2$ remains (semi)metallic. PtS_2 on the other hand is semiconducting in the bulk and consequently no metal to semiconducting transition is observed as a function of the number of layers. Experimentally, the semiconducting behavior of monolayer $PtTe_2$ and for mono- and bilayer- $PtSe_2$ was found recently by angle resolved photoemission spectroscopy (ARPES) measurements.[25,26,27] However, the band gap cannot directly be determined from valence band measurements alone. Here, we study the properties of these nanoscale Pt-dichalcogenides by scanning tunneling microscopy (STM) and spectroscopy (STS) and correlate these experimental results to properties derived by DFT calculations.

Results and discussion

$PtSe_2$ and $PtTe_2$ have been synthesized on graphitic substrates by molecular beam epitaxy at growth temperatures of 240-260 °C. For STM and STS characterization the Pt-dichalcogenides were grown on highly oriented pyrolytic graphite (HOPG). ARPES studies of $PtTe_2$ were performed on bilayer graphene/SiC(0001) substrates. For transmission electron microscopy (TEM) characterization Pt-dichalcogenides were grown directly on a graphene-covered TEM grid. While transfer of CVD grown TMDs to TEM grids for their analysis is common practice, the direct MBE growth on graphene on a TEM grid enables additional characterization of the growth such as epitaxial alignment between the substrate (graphene) and the Pt-dichalcogenides.

Phase characterization: Pt-dichalcogenides are expected to form the 1T-phase. However, previous reports for ultrathin films have also implicated a 2H phase,[28] and the possibility of nanostructured monolayers with both 1T and 1H grains has been demonstrated for $PtSe_2$.[29] Moreover, Pt-tellurides may exist in various compositional phases from mono- to di-tellurides.[30,31] The high vapor pressure of chalcogens makes a prediction of the compositional phase difficult and it may sensitively depend on the MBE growth conditions. As different phases are conceivable, it is necessary to confirm the composition and phase obtained under the conditions employed in this study.

Initial characterization of the phase of the films grown here was done by x-ray photoemission spectroscopy (XPS). Pt-selenide and tellurides were grown on HOPG. Fig. 1 shows XPS data for the Pt-4f, and Se-3d or Te-3d peaks for Pt-selenide and Pt-telluride films, respectively. The peak positions are referenced relative to the C 1s peak, set to 284.8 eV. A Shirley background is subtracted, and all peaks are fitted with Voigt functions. The Pt-$4f_{7/2}$ / $4f_{5/2}$ binding energies are measured at 73.4 / 77 eV and 72.8 / 76.4eV for Pt-selenide and Pt-telluride, respectively. The binding energies for Se- $3d_{3/2}$ / $3d_{1/2}$ are determined at 54.9 /55.8 eV, and the binding energy for Te- $3d_{3/2}$ / $3d_{1/2}$ are found at 573.4 / 583.9 eV. The 0.6 eV chemical shift of the Pt peaks for the two dichalcogenides is consistent with the larger electronegativity of Se compared to Te. Generally, the peak position of Pt agrees with reports for Pt-dichalcogenides,[32,33] suggesting the successful synthesis of $PtSe_2$ and $PtTe_2$. To further verify the phase, we performed *ex-situ* TEM characterization.

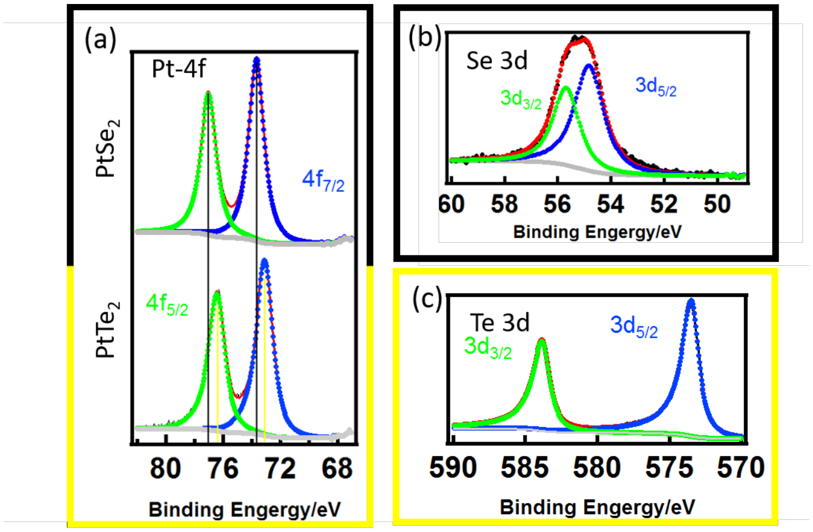

Figure 1: X-ray photoemission characterization of MBE grown Pt-dichalcogenides. (a) Pt-4f core levels for $PtSe_2$ (top) and $PtTe_2$ (bottom). The core level binding energies (BE) are shifted by 0.6 eV to higher BE for $PtSe_2$ compared to $PtTe_2$. The Se-3d core level is shown in (b) and Te-3d core level in (c).

To characterize MBE grown Pt-chalcogenides by TEM, the films were directly grown on suspended graphene on a TEM grid. Prior to the growth, the TEM grid was outgassed in UHV by annealing to 300 °C for 12 h and then the Pt-chalcogenides were deposited under the same conditions as on the other growth substrates. Subsequently to the growth, the samples were taken out of the UHV growth chamber for TEM analysis. The samples were annealed in the TEM to desorb some adsorbates from the air-exposure at 200 °C for 30 min, but nevertheless additional carbon was detected decorating the $PtSe_2$ and the $PtTe_2$ edges. TEM characterization confirmed the formation of the Pt-chalcogenides on the graphene sheet in an island growth mode. On large-scale images two regions are observed with distinctively different island sizes as can be seen in Fig. 2 (a). This is likely a consequence of local contamination on the graphene/TEM grid that affects the nucleation and growth in some regions. The distribution of lateral island areas is about 30-100 nm^2 in one region and 100-650 nm^2 in the other. The regions with the smaller islands are similar to those grown *in situ* on HOPG and observed by STM (discussed below) and thus these regions are deemed to have been contamination-free during growth, while the larger islands are likely formed by adsorption and agglomeration at pre-existing contamination on the graphene. All the regions show carbon contamination, which is expected to have occurred during post-growth air exposure. The island heights vary from monolayer to multilayers. HRTEM images of bilayer islands are shown in Fig 2 (c). While the image contrast allows to exclude the possibility of the 2H phase for both monolayer and bilayers, the contrast differences between different stackings of the 1T layers in bilayers, *i.e.*, 1T or 3R stacking, is very small (see Fig. S1) and does not allow to unambiguously differentiate between these stackings from image contrast alone. However, the Se and Pt sublattices and the number of layers were identified from frequently observed Se-vacancies, by analyzing line scans along Pt and Se atoms as shown in Fig S2. Importantly, the HRTEM-images (see Fig 2) in combination with the line-scans (Fig S2) as well as the simulated images of different possible structures (see Fig, S1) confirm the formation of bilayer $PtSe_2$ with 1T-structure. While this identifies specific islands, the small imaging contrast to the 3R stacking does not allow us to exclude the possibility of the presence of 3R stackings anywhere in the sample. DFT calculations including many-body dispersion corrections to account for weak van der Waals interactions, however, indicate the preference of the 1T stacking in bilayers (Fig. S3). Thus, DFT and selected TEM image analysis are consistent with a majority of 1T stacked bilayer islands. Fourier transformation shown in Fig. 2(b) also demonstrates that the $PtSe_2$ islands have a lattice constant of $a_{PtSe2} = 0.38$ nm, consistent with the previously reported data.[34,35] Interestingly, despite the weak van der Waals interactions between graphene and $PtSe_2$, the $PtSe_2$-islands grow epitaxially on the graphene substrate, *i.e.*, the hexagonal lattice of the islands is aligned with respect to the hexagonal structure of graphene. This is apparent from the Fourier transform that shows both the periodicity of the substrate and the Pt-chalcogenide islands. HRTEM images of MBE-grown $PtTe_2$ islands are similar in many respects to those of $PtSe_2$ as evident from Fig. 2 (d). The imaging contrast of the flake may vary slightly in different regions of the image which originates from slight focus variations over the imaged surface area as well as contamination. Moreover, at the edges of the flake (near the corners of the image) the hexagonal structure from underlying graphene support is visible. The $PtTe_2$ monolayer islands could also be identified as 1T-phase with a lattice constant of 0.41 nm. Also, an epitaxial relationship with the graphene substrate was observed. While HRTEM confirms the phases of the MBE grown Pt-dichalcogenides as 1T, the layer dependent band gaps were characterized by STM/STS as well as ARPES studies for $PtTe_2$.

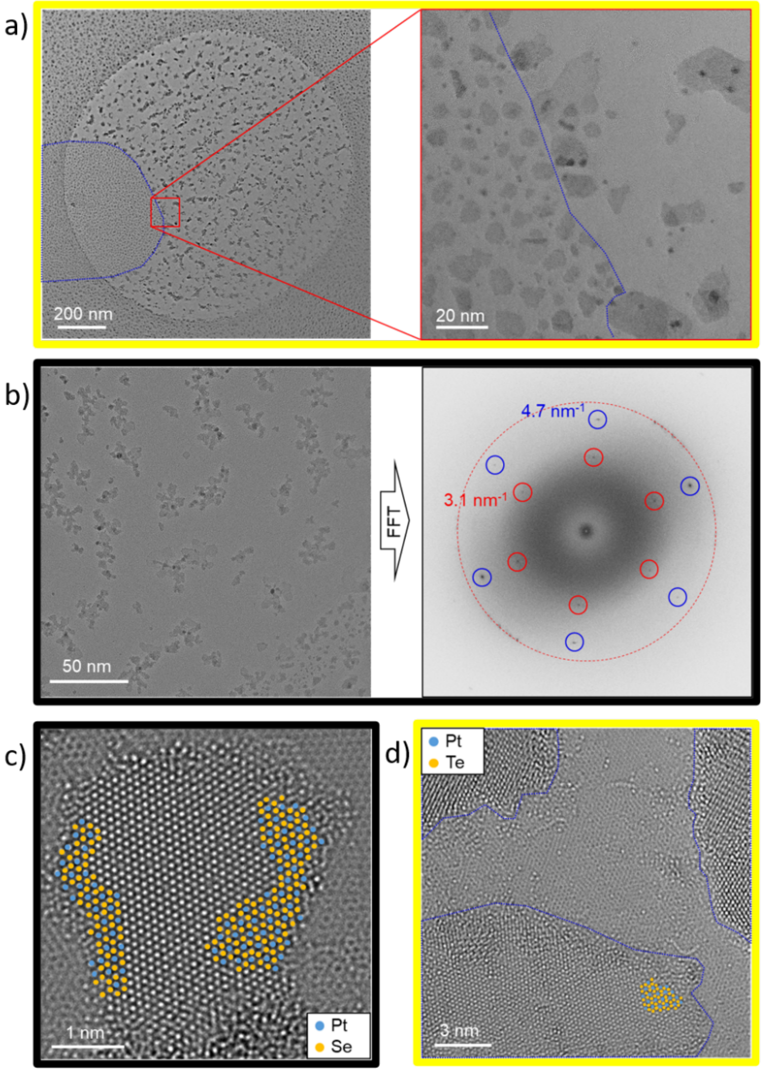

Figure 2: Cc/Cs-corrected HRTEM analysis of Pt-chalcogenides directly grown on graphene supported on a TEM grid. (a) large scale TEM image showing a region of suspended graphene over a TEM grid. Clearly there are two regions with different island morphology. The region with smaller, more uniformly distributed islands is associated with the growth on a contamination free surface. In a second region, larger islands are observed, which is associated with nucleation and growth at surface contamination. (b) shows a zoomed in TEM image of Pt-selenide islands on graphene. The fast Fourier transformation (FFT) shows the reciprocal lattice points for graphene (blue circles) and Pt-selenide (red circles). The rotational alignment of the reciprocal lattice of the graphene substrate and that of the $PtSe_2$ islands show that $PtSe_2$ grows mainly in an epitaxial relationship. Second order reflections of $PtSe_2$ are located along the red dotted circle. Moreover, the lattice constant of Pt-selenide is determined from the Fourier transform to ~0.38 nm, which is consistent with the lattice constant of $PtSe_2$. The FFT was inverted for better visibility. High resolution TEM image of a $PtSe_2$ bilayer island is shown in (c). The Pt and Se sublattices are indicated and it shows that the structure is consistent with the 1T phase of transition metal dichalcogenides. Similarly, the crystal structure of $PtTe_2$ can be confirmed to be 1T from the HRTEM image shown in (d). Data with a yellow frame correspond to $PtTe_2$ samples and black frames show data from a $PtSe_2$ sample.

Layer dependent electronic properties: MBE grown Pt-dichalcogenide islands on conducting HOPG-substrates are well-suited for probing the local electronic structure by STS. Islands of Pt dichalcogenides with different number of layers allows to directly probe the band gap on different terraces and thus reveal the layer dependent properties. Fig. 3 presents large scale STM images of $PtSe_2$ and $PtTe_2$ islands grown on HOPG. The cross-sectional scan shows that these islands exhibit terraces with different number of layers.

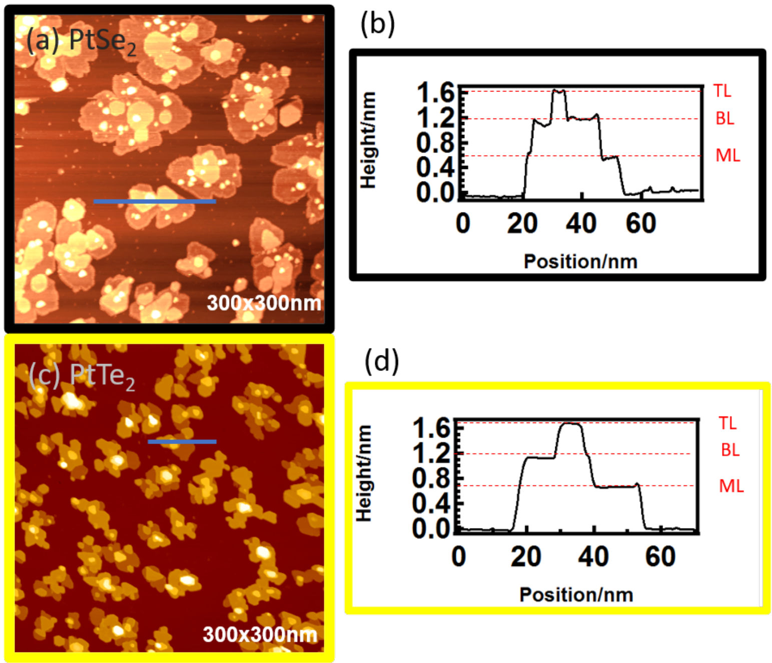

Figure 3: Large scale STM images of Pt-dichalcogenide islands grown by MBE on HOPG substrates. (a) and (b) show an STM image and corresponding line profile for $PtSe_2$ islands. (c) and (d) present an STM image and line profile for $PtTe_2$ islands. The line profiles are shown along the line indicated in the corresponding STM images. It can be seen that typical islands expose mono-(ML), bi- (BL), and tri-layer (TL) terraces, which enables characterization of the layer dependent electronic properties by STS.

The apparent step height of the first layer, *i.e.* the step from the HOPG substrate to the Pt-dichalcogenide is strongly bias voltage dependent because of the semiconducting nature of the monolayer. For $PtSe_2$, for example, we measure apparent heights as small as 0.3 nm for bias voltages close to the band gap (in a range of -1V to +0.3 V) while at larger bias voltages (larger than +0.5 V) a step height of 0.8 nm is measured. In the latter case we tunnel into the empty states of the film and the measured height is closer to the true topographical height of the first layer on HOPG. This would indicate a large van der Waals gap between the HOPG and the Pt-dichalcogenides, comparable to what has been reported for other TMDs grown on graphitic substrates. Similar to the monolayer, the step height to the bi-layer is again dominated by electronic effects for small bias voltages. At larger bias voltages the bi-layer step height is deemed to be less affected by electronic effects and a step height of 0.50±0.03 nm is determined. This value corresponds to the interlayer separation in $PtSe_2$, which is discussed in more detail below in connection to the DFT calculations. Atomic resolution images of monolayer $PtSe_2$ on HOPG show a 2×2 superstructure but not for multilayers. Figure 4 (a) and (b) present the atomic resolution STM images of such monolayer samples. HRTEM of samples grown under the same conditions indicate that the monolayer is 1T-$PtSe_2$. Moreover, HRTEM demonstrated the rotational alignment between graphite and $PtSe_2$ and 3 times the lattice constant of HOPG ($3\times a_{HOPG} = 0.74$) corresponds closely to 2 times the lattice constant of $PtSe_2$ ($2\times a_{PtSe2} = 0.76$). Therefore, we assign the 2×2 structure observed in STM to a moiré superstructure due to a close-to-coincidence lattice between the HOPG substrate and $PtSe_2$. The superpositioning of the graphene lattice with the lattice of $PtSe_2$ is schematically shown in Fig. 4 (a), illustrating the formation of a 2×2 structure. Further evidence that $PtSe_2$ on HOPG is forming a moiré superstructure comes from the occasional observation of minority structures that originate from a rotation of the $PtSe_2$ with respect to the substrate. In these domains a much larger moiré superstructure with a $\sqrt{13}\times\sqrt{13}$-R13.9° unit cell with respect to the $PtSe_2$ structure is observed. An example of such a structure is shown in Fig. 4 (c). Moiré supercells in $PtSe_2$ was previously reported for monolayers on Pt(111) substrates,[36] but the interaction with graphite is expected to be significantly weaker than with a transition metal surface. For $PtTe_2$ on HOPG substrates, a 3×3 moiré structure is observed for bias voltages around +0.5 V in STM images, shown in Fig. 4 (d), which can be interpreted with a near-coincidence lattice of $3 \times a_{PtTe2} \sim 5 \times a_{HOPG}$. Below we calculate the interaction between graphene and $PtSe_2$ and find very weak interactions, which suggests that the observed moiré pattern in STM images may not be due to a physical distortion of the Pt-dichalcogenides but are rather imaging effects through resonant tunneling in Pt-dichalcogenide/ graphene electronic states. This is further supported by the strong bias voltage effect in $PtTe_2$ that allows to observe a moiré pattern only for a narrow voltage range.

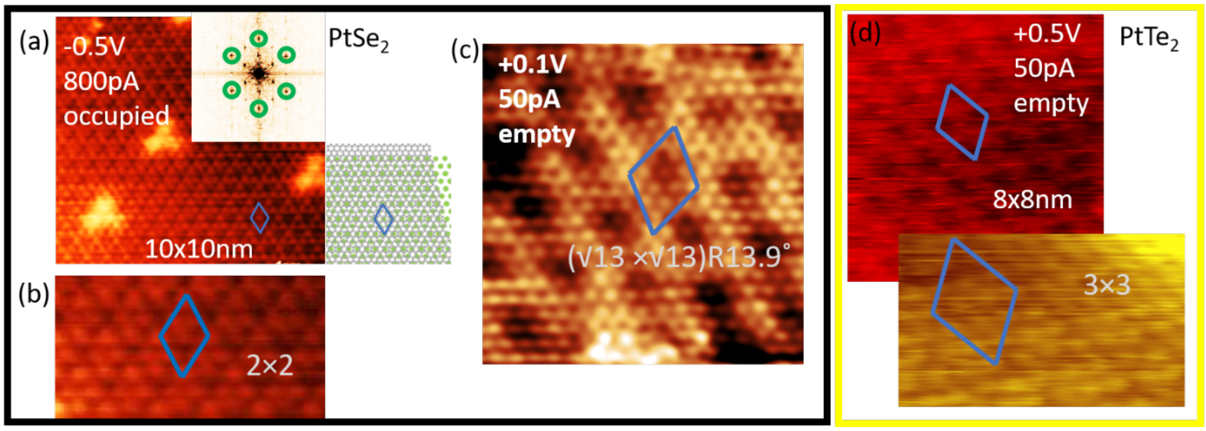

Fig. 4: STM characterization of monolayer $PtSe_2$ and $PtTe_2$ grown on HOPG. Monolayer $PtSe_2$ exhibits a 2×2 superstructure in STM images as shown in (a). The inset shows the Fourier transform of the STM image. The 1×1 reciprocal lattice points are indicated by green circles. The additional spots indicate the 2×2 superstrucutre. This superstructure is considered the result of a moiré structure, schematically illustrated in (a) by superimposing the graphene atomic crystal (gray circles) with lattice points of the $PtSe_2$ (green circles). It can be seen that three unit cells of graphene almost match two unit cells of $PtSe_2$. Although the structure is not completely commensurate a 2×2 superstructure emerges. A zoom-in image of the STM image of $PTSe_2$ monolayer is shown in (b). On rare occasions a different superstructure with a √13×√13 R13.9 periodicity is observed, shown in (c). This is considered to be due to a rotation of the $PtSe_2$ grain relative to the graphene substrate. Monolayer $PtTe_2$ exhibits a 3×3 superstructure in STM if imaged with a 0.5 V bias voltage, as shown in (d).

Fig. 5 shows STM images of $PtSe_2$ and $PtTe_2$ islands that exhibit terraces with mono-, bi-, and tri-layer thickness. STS measurements on these three regions indicate strong changes in the band gap. In $PtSe_2$ the monolayer exhibits a large gap of 1.79±0.04 eV, which shrinks to 0.62±0.02 eV for the bilayer and the sample becomes metallic for the trilayer. The uncertainty represents the standard deviation from around 50 datapoints for the monolayer and around 25 datapoints for bi-trilayer samples, where each datapoint is the average of 9-16 spectra. In addition to measurements of different islands of the same sample, we were also conducting measurements on different samples grown with slightly varying coverage that allows to obtain larger terraces. An example for STS on larger top terraces is shown in supplemental Fig. S4 for PtSe2. Within the range of terrace sizes of up to 100's of nanometer in diameter we do not see a variation of the band gap at the center of the terraces, while a variation is observed towards the edges of the islands. In contrast, $PtTe_2$ exhibits a band gap of 0.51± 0.02 eV only for the monolayer, while the bi- and tri-layer are metallic. The measurement of $PtTe_2$ follow similar statistics as for $PtSe_2$ and additional data for larger terraces are shown in Fig. S5. To compare the valence band edge in STS with band structure measurements, we also grew $PtTe_2$ on graphene/SiC and performed ARPES measurements with our in-house set-up using a He-II source. Fig. 6(a) shows the ARPES data for predominantly monolayer samples (with some bilayer regions) as can be seen from the STM images of the corresponding sample, presented in Fig. 6 (b). ARPES for bilayer samples show the metallic character of the sample with bands crossing the Fermi-level. Our STS data for monolayer also compare well with the ARPES data, with the valence band maximum at Γ in ARPES coinciding with the band onset in the STS spectra as illustrated in Fig. 6(c). Note that there is additional photoemission intensity visible within the band gap of the ARPES data, which is associated with the existence of some metallic bilayer islands in the sample, which was confirmed by STM imaging of the sample. ARPES measurements on predominantly bilayer samples are shown in Fig. 6 (d), which highlights the presence of a metallic band.

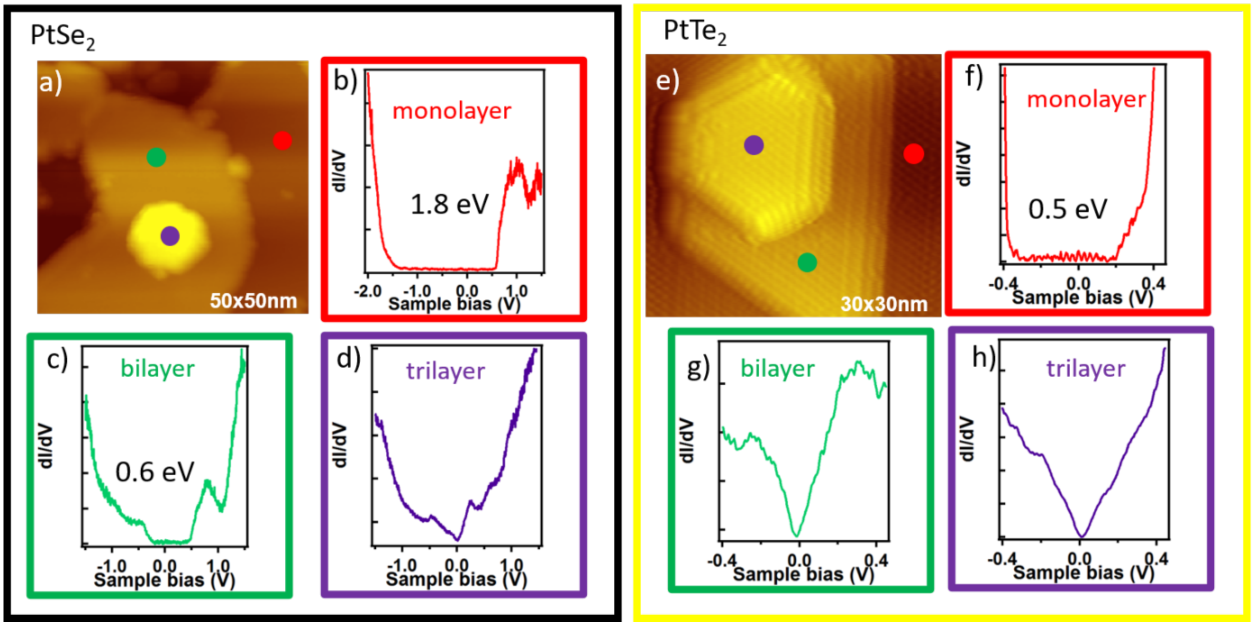

Figure 5: Layer dependent band gap measured by STS. (a) STM image of a $PtSe_2$ island with different layer heights. The points for STS measurements are indicated by the colored dots and the corresponding dI/dV spectra are shown for the monolayer (b), bilayer (c), and trilayer (d) regions. STM images of a $PtTe_2$ island with different terrace height is shown in (e) and the corresponding dI/dV spectra for monolayer (f), bilayer (g) and trilayer (h) regions are shown. The measured band gaps are given in the STS spectra. STS have been taken with a set-point of 0.7 V and 50 pA.

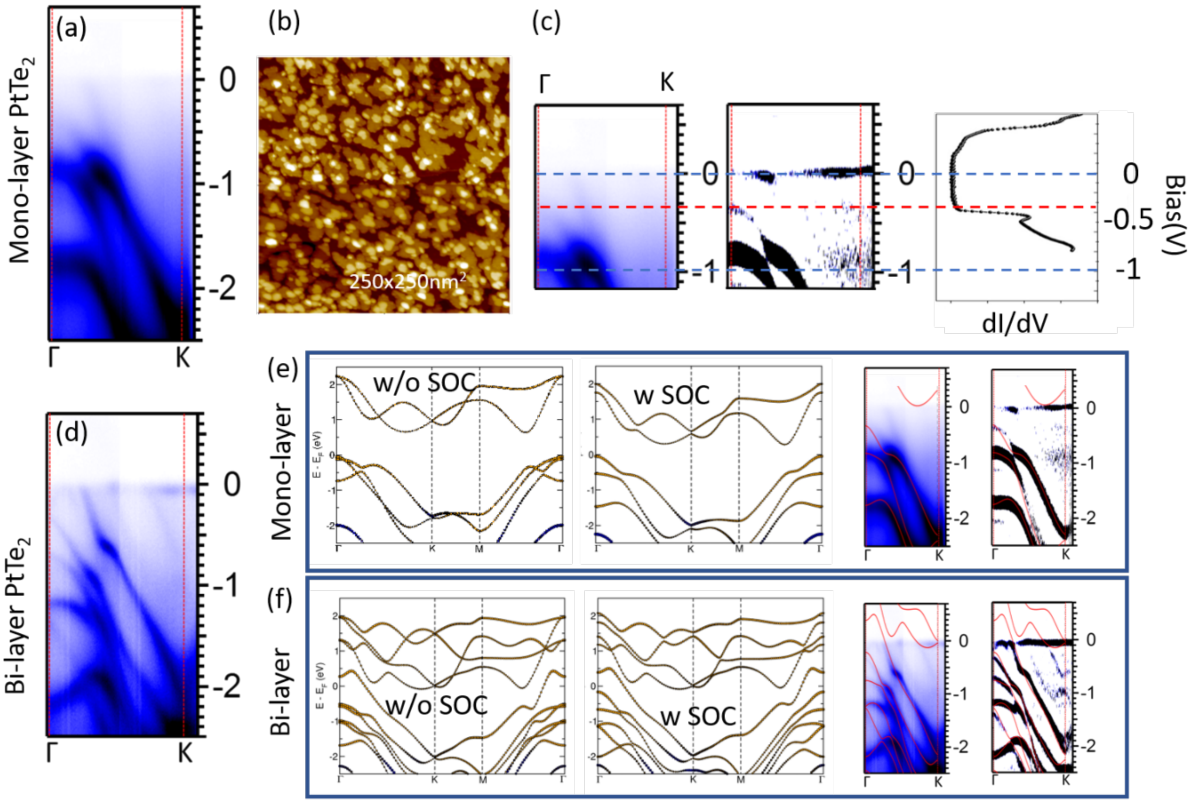

Figure 6: ARPES measurement of PtTe$_2$ grown on graphene/SiC, its comparison with STS measurements for monolayer PtTe$_2$ on HOPG, and with DFT simulations. (a) ARPES of monolayer, with some bilayer islands as the STM characterization (b) of the sample indicates. (c) shows the comparison of the STS data for monolayer with the ARPES measurements. The VBM at Γ (better seen in the second derivative of the ARPES data) coincides closely with the intensity onset in the STS spectra. Additional intensity in the ARPES spectra away from the Γ point are attributed to the bilayer regions on the sample. This is justified by a comparison to the ARPES spectra of the bilayer sample shown in (d). These bilayer samples show a metallic band that intersects the Fermi-level in between Γ-K. DFT simulations for mono- and bi-layer PtTe$_2$ are shown in (e) and (f), respectively. It is apparent that inclusion of SOC is required to gain agreement with the experimental ARPES measurement, as the overlay of DFT band structure with the experiment shows.

In order to rationalize the experimental observations, we carried out DFT calculations as detailed in the Methods section. The 1T structure has been expected to be thermodynamically most stable phases for both PtSe$_2$ and PtTe$_2$,[37] and this has been confirmed in our sample characterization. It is worth pointing out that monolayer 1H phase would exhibit metallic charactered according to our DFT simulations shown in Fig. S6 and thus no band gap opening would be expected. Thus, in the following only the 1T structure is considered in our calculations. The optimized lattice constants were found to be in good agreement with the experimental values, as presented in Table S1. To test our theoretical approach further, we compared calculated band structures with the experimental ARPES data for $PtTe_2$ mono- and bi-layer samples (comparable calculations for 1T-$PtSe_2$ are shown in the supplemental information in Fig. S7). It is apparent that good agreement with the experimental band structure is obtained only if spin orbit coupling (SOC) is included in the calculations as shown for the monolayer in Fig. 6 (e) and the bilayer in Fig. 6 (f). An overlay of the experimental band structure with the calculated bands is also shown. The good agreement validates the DFT approach. The calculations indicate that monolayer $PtTe_2$ and $PtSe_2$ exhibits an indirect band gap, with the VBM at the Γ point and the CBM at low symmetry points along the Γ-M direction. However, as we show next, the magnitude of the band gap determined from DFT can vary significantly depending on the approach.

Before we turn to the computational band gap values, we first examine if the graphene substrate plays a role in the experimental band gap measurements. Band gap renormalization for TMDs on metal supports have been discussed extensively mainly for the Mo-dichalcogenides.[38] Clearly, on pure transition metals, such as Au, a strong decrease of the fundamental band gap compared to free standing material is observed.[39] On weakly interacting substrates such as graphene or graphite the situation is less clear, though. For MoS_2, for example, the measured gaps vary between 2.15 - 2.4 eV for graphite[40,41] or 2.53 eV for graphene/Ir[42] substrates, while some DFT calculations predict gaps as large as 2.8 eV for the monolayer.[43,44] However, the used DFT method may cause an overestimation of the gap value and thus the reduced experimental gap may not be direct evidence of a substrate induced gap narrowing. Nevertheless, the spread of the experimental values may indicate that subtle effects on growth conditions and substrate properties can affect the gap values. Thus, similarly to the studies on MoS_2, more studies by others on different substrates are needed to clarify how robust the experimental gap values for Pt dichalcogenides are. Next, we show that on a pure DFT level the band gap value of monolayer $PtSe_2$ is not affect by a graphene substrate. The $PtSe_2$/graphene heterostructure is constructed with 3 × 3 unit cells of graphene and 2 × 2 unit cells of $PtSe_2$ monolayer corresponding to a lattice mismatch of only 0.7%. (Fig. 7). Structural optimization with many-body dispersion correction leads to an average interlayer distance of $d = 3.47$ Å between $PtSe_2$ and graphene. We have also checked different stacking orders between graphene and $PtSe_2$, by varying the lateral orientation of the layers along the armchair and zigzag directions of graphene. The results indicate an energy variance of just 0.1-2.8 meV suggesting weak uniform interactions between the components. The band structure of the heterostructure shows the linear energy dispersion close to the Fermi level resembling the Dirac cone of graphene. The projected densities of states suggest that the band gap of $PtSe_2$ monolayer on graphene is very similar to that of the free-standing monolayer, indicating that Pt-dichalcogenides supported on graphitic substrates are good models for qualitative analysis of the electronic properties of free-standing layers. To further test the influence of the substrate on the band gap, the separation between graphene and $PtSe_2$ was artificially reduced by up to 10% of its equilibrium separation and the gap value was re-evaluated. The results are presented in Fig. S8. No substantial effect was found with the gap changing by less than 0.03 eV. We note though, that the states in the conduction band will be likely shifted upwards in the experiment, as DFT/PBE underestimates the gap. It is also noteworthy that interface band alignment in the graphene/$PtSe_2$ system causes a slight shift of the Fermi-level towards the conduction band in the DFT calculations associated with small charge transfer to $PtSe_2$, see Fig. S9. This is similar to the slight *n*-type doping we measure experimentally for $PtSe_2$ monolayers by STS shown in Fig. 5 (b).

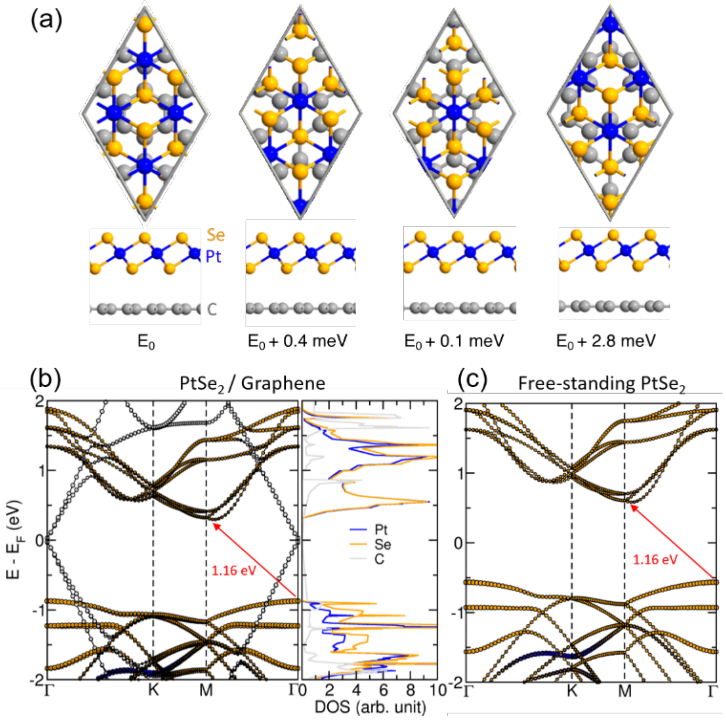

Fig. 7: (a) Schematics of atomic structures (bottom and side views) of $PtSe_2$/graphene interfaces in several stacking configurations. The energy difference (for the whole system) with respect to the lowest energy configuration is given. (b) Comparison of band structure calculations for freestanding $PtSe_2$ with that on a graphene substrate, indicating the negligible modification of the $PtSe_2$ band structure by the presence of a graphene substrate.

Our electronic structure calculations using PBE functional show that $PtSe_2$ and $PtTe_2$ monolayers have indirect band gaps of 1.20 eV and 0.33 eV, respectively. Applying quasi-particle band-gap calculations at the G_0W_0 level increases the band gap of $PtSe_2$ ($PtTe_2$) to 2.44 eV (1.29 eV). These values are normally overestimations of the band gaps for the free-standing monolayers.[45] As PBE usually underestimates band gaps, we can assume that the experimental values are between the PBE and the G_0W_0 values, in agreement with the experimental data. The calculated band gaps are also in good agreement with the previously reported values at a similar level of theory.[14,36] Increasing the number of layers from mono to bilayer leads to a significant reduction of the calculated band gaps and gives rise to a semi-metallic behavior for the trilayer and beyond (Table 1), confirming the strong interlayer interaction in these materials.

	1L	2L	3L	4L
$PtSe_2$				
PBE (SOC) G_0W_0 (SOC)	1.20 eV 2.44 eV	0.22 eV 1.174 eV	0.01 eV 0.30 eV	0 eV 0 eV
DFT (ref.[14])	1.18 eV	0.24 eV	-0.08 eV (semi-metallic)	-0.29 eV (semi- metallic)
STS Experiment	1.79 ± 0.04 eV	0.62± 0.02 eV	0 eV	0 eV
$PtTe_2$				
PBE (SOC) G_0W_0 (SOC)	0.33 eV 1.29 eV	0 eV 0 eV	0 eV 0 eV	0 eV 0 eV
DFT (ref. [14])	0.4 eV	-0.51 eV (semi-metallic)	-0.94 eV (semi-metallic)	-1.06 eV (semi-metallic)
STS Experiment	0.51 ± 0.02 eV	0 eV	0 eV	0 eV

Table 1: Computed and experimentally determined band gap values in $PtSe_2$ and $PtTe_2$ as a function of number of layers.

In the case of multilayer systems, however, the chosen vdW correction method has a major influence on the calculated band gap. While the DFT+D3 method turns out to underestimate the distance between layers, more advanced TS and MBD corrections increase the interlayer distance approaching the experimental range of 5.08-5.3 Å. To further evaluate the dependence of band gaps on the applied level of theory, we systematically changed the interlayer distance and recalculated the band gaps at PBE, HSE and GW levels (Figure 8 a), and found a strong dependence on interlayer separation, which may explain the differences in the previously reported theoretical values of the gap, as different methods of accounting for vdW interaction give different results. It has been shown that the VBM and CBM states are mainly contributed from the Se-p_z orbitals, normal to the lattice plane which are sensitive to the interlayer separation,[15] which in turn, affects the gap value.

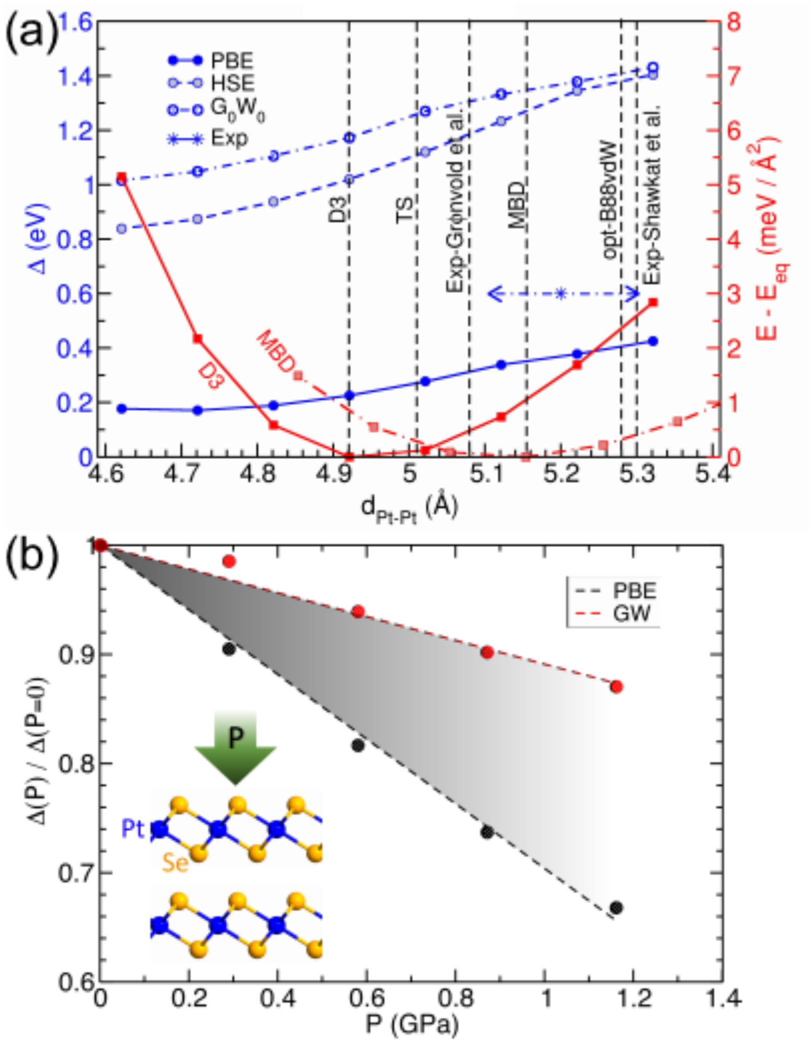

Fig. 8: (a) Band gap energy (Δ) versus interlayer distance (d_{Pt-Pt}) in $PtSe_2$ bilayer calculated at the DFT/PBE level with account for vdW interaction, HSE and GW levels. The experimental values, reported in Refs. [46] and [47], are given for comparison. (b) Relative change in the band gap (Δ) as a function of compressive pressure (P).

Keeping in mind the strong dependence of the band gap in $PtSe_2$ and $PtTe_2$ on the interlayer separation, we further investigated the response of bilayer system under compression applied perpendicular to the surface. The $PtSe_2$ bilayer was subjected to a normal compressive load in a 'displacement regulation simulation,' in which the equilibrium interlayer distance is systematically reduced in steps and the total energy is recalculated. The energies and the area of the interface were used to calculate the applied pressure (P) at each step. The band gap evolution under applied compression indicates almost linear behavior with increasing pressure (Fig. 8 b). The band gaps calculated at the PBE level were found to be more sensitive to the pressure than those from G_0W_0 method. The slope of this band gap *vs*. pressure curve (the band gap normalized to the gap without external pressure) about 28% (11%) per 1 GPa of pressure at the PBE (G_0W_0) levels. The pressure-induced band gap change is $PtSe_2$ is more pronounced in comparison to group-VI TMDs such as $MoSe_2$,[48] suggesting that noble TMDs are promising materials for pressure-tunable optoelectronic devices or sensors.

Conclusions

The 1T Pt-dichalcogenides can be grown by MBE as epitaxially aligned islands on various graphitic substrates. On HOPG, individual islands expose multiple terrace heights thus enabling to measure the electronic properties variation as a function of the number of layers by STS. For $PtSe_2$ a transition from a metal for more than 3-layers thick islands to a semiconductor is observed, while for $PtTe_2$ the transition from metal to semiconductor occurs only for the monolayer. The fundamental band gaps have been determined experimentally by STS which show that monolayers of $PtSe_2$ and $PtTe_2$ exhibit significant indirect band gaps of 1.8 eV and 0.5 eV, respectively. DFT calculations reproduce the general trend of opening of a gap as the number of layers are reduced, but band gap values depend strongly on the theoretical approach and can differ significantly from the experimentally determined band gaps. The strong layer dependence of the fundamental band gap in $PtSe_2$ and $PtTe_2$ is attributed to interlayer interactions, which are stronger than in other TMDs. This sensitivity of the band gap to interlayer separation also let us to propose that the band gap can be tuned by uniaxial compression of the bilayer systems. Our theoretical studies suggest that significant modifications of the band gap can be obtained in bilayer $PtSe_2$ with modest pressure of less than 1 GPa, making it a feasible system for stress sensors or stress-tunable optoelectronic devices.

Methods:

Experimental details: (Sub) monolayer $PtSe_2$ and $PtTe_2$ is grown by MBE on graphene or graphite. For HRTEM studies CVD-grown graphene was transferred to a TEM grid. Prior to MBE growth on such substrates the graphene/TEM grid was annealed in ultra-high vacuum (UHV) at 300 °C for 12 h. For ARPES studies single crystalline bilayer graphene was obtained on a 6H- SiC(0001) substrate by vacuum annealing. This substrate allows for TMDs to grow with a single orientation and thus enables angle resolved studies. In contrast graphite (HOPG) substrates have twist domains and thus are less well suited for angle dependent studies but are suitable for STM work. The HOPG substrates are freshly cleaved in air and outgassed at 450 °C in vacuum for 12h. $PtSe_2$ and $PtTe_2$ are grown in to separate UHV chambers dedicated to selenide and telluride growth respectively. In both chambers, Pt is evaporated from a 2 mm Pt rod in water-cooled mini e-beam evaporators and the chalcogens are evaporated from water-cooled Knudsen cells. During deposition the substrate temperature was held at 240 to 260 °C. The telluride growth chamber was connected via a vacuum transfer to a surface analysis UHV chamber equipped with RT-STM, ARPES, x-ray photoemission spectroscopy, and low energy electron diffraction (LEED) for sample characterization. The selenide growth chamber had a large sample to source distance, which reduced the growth rate and allowed only for a growth rate of 0.33 ML/h estimated from STM images. The growth chamber was connected to a RT Omicron STM and samples were transferred to another UHV chamber for XPS analysis. STS measurements were conducted in a dedicated low temperature STM/STS with a closed cycle cooling system. $PtSe_2$ and $PtTe_2$ were transferred to this chamber through air or using a vacuum suitcase. The sampled were annealed to 200 °C in the UHV chamber prior to STS studies. Electrochemically etched tungsten tips were used for STS. dI/dV spectra were recorded using a lock-in amplified with a modulation voltage of 30 mV.

HRTEM were conducted on $PtSe_2$ and $PtTe_2$ directly grown on a graphene covered TEM grid. The graphene was grown by CVD on a copper foil and transferred to the TEM grid. The grown samples were exposed to air but packed in an inert gas atmosphere for shipping to the TEM facility. Before TEM analysis the samples were annealed to 200 C in vacuum. The TEM images were acquired with the Cc/Cs-corrected Sub-Angstrom Low-Voltage Electron Microscope (SALVE), which was used at an acceleration voltage of 80 kV. Measured values for chromatic and spherical *aberrations were in the range of -10 to -20 µm. Used dose rates for the atomic resolved images were in the range of 10^6 e^-/nm^2s. The images were recorded with a 4k x 4k Ceta camera with exposure times of 1s.*

Computational details: Density-functional theory (DFT) calculations were performed within the projector augmented wave method as implemented in VASP code[49]. The generalized gradient approximation (GGA) proposed by Perdew-Burke-Ernzerhof (PBE) was used as the exchange-correlation functional [50]. The plane wave calculations are performed with an energy cutoff of 600 eV. The Brillouin zone of the system was sampled using 12× 12 × 1 k-mesh for monolayer and 12 × 12 × 12 k-mesh for bulk materials. The long-range vdW interactions were taken into account using DFT-D3[51], optB88vdW[52], and many-body dispersions[53]. HSE06 calculations were carried out using Heyd-Scuseria-Ernzerhof hybrid functional.[54],[55]The calculations of quasiparticle energies and eigenvalues were performed by applying single-shot GW on the self-consistent DFT/PBE ground-state calculations.[56],[57] The GW bandgap energies were converged with a respect to the empty states and 512 empty bands were applied for all the calculations. A 6 × 6 × 1 k-point is used with all G-vectors included in the GW calculations. All the electronic structure calculations included the spin-orbit coupling (SOC) effect.

Supporting Information:

The supporting information is available free of charge at: http://pubs.acs.org/doi/XXXXXXX

Figure S1: High resolution TEM image simulation for 1T, 2H, and 3R phases of $PtSe_2$.

Figure S2: TEM structure identification *via* Se-vacancies

Figure S3: Calculated energies of bilayer PtSe2 with different stacking.

Figure S4: Additional STS data for $PtSe_2$.

Figure S5: Additional STS data for $PtTe_2$.

Table S1: comparison of DFT lattice constant to experimental values.

Figure S6: Electronic structure calculations for metallic H-phase $PtSe_2$.

Figure S7: Electronic structure calculations for $PtSe_2$ with and without spin orbit coupling.

Figure S8: Electronic structure of $PtSe_2$/graphene with artificially altered layer separation.

Figure S9: Calculated charge transfer between $PtSe_2$ and graphene.

Acknowledgements:

We acknowledge funding from the German Research Foundation (DFG), project KR 48661/1, and through the collaborative research center “Chemistry of Synthetic 2D Materials” SFB-1415-417590517. We further thank the Gauss Centre for Supercomputing e.V. (www.gauss-centre.eu) for providing computing time on the GCS Supercomputer HAWK at Höchstleistungsrechenzentrum Stuttgart (www.hlrs.de) and also TU Dresden (Taurus cluster) for generous grants of CPU time. The USF group acknowledges financial support from NSF through award 1801199 and 2140038.

References:

---

[1] Wilson, J.A.; Yoffe, A.D. The Transition Metal Dichalcogenides Discussion and Interpretation of the Observed Optical, Electrical and Structural Properties. *Adv. Phys.* **1969**, *18*,193-335.

[2] Manzeli, S.; Ovchinnikov, D.; Pasquier, D.; Yazyev, O.V.; Kis, A. 2D Transition Metal Dichalcogenides. *Nat. Rev. Mater.* **2007**, *2*, 17033.

[3] Lasek, K.; Li, J.; Kolekar, S.; Coelho, P.M.; Zhang, M.; Wang, Z.; Batzill, M. Synthesis and Characterization of 2D Transition Metal Dichalcogenides: Recent Progress from a Vacuum Surface Science Perspective. *Surf. Sci. Rep.* **2021** DOI: 10.1016/j.surfrep.2021.100523.

[4] Mak, K. F.; Lee, C.; Hone, J.; Shan, J.; Heinz, T.F. Atomically Thin MoS_2: A New Direct-Gap Semiconductor. *Phys. Rev. Lett.* **2010**, *105*, 136805.

[5] Kolekar, S.; Bonilla, M.; Ma, Y.; Diaz, H.C.; Batzill, M. Layer-and Substrate-Dependent Charge Density Wave Criticality in 1T–$TiSe_2$. *2D Mater.* **2017**, *5*, 015006.

[6] Chen, P.; Pai, W.W.; Chan, Y.-H.; Takayama, A.; Xu, C.-Z.; Karn, A.; Hasegawa, S.; Chou, M.Y.; Mo, S.-K., Fedorov, A.-V.; Chiang T.-C. Emergence of Charge Density Waves and a Pseudogap in Single-Layer $TiTe_2$. *Nat. Commun.* **2017**, *8*, 516.

[7] Coelho, P.M.; Cong, K.N.; Bonilla, M.; Kolekar, S.; Phan, M.-H.; Avila, J.; Asensio, M.C.; Oleynik, I.I.; Batzill. M. Charge Density Wave State Suppresses Ferromagnetic Ordering in VSe_2 Monolayers. *J. Phys. Chem. C* **2019**, *123*, 14089-14096.

[8] Duvjir, G.; Choi, B.K.; Jang, I.; Ulstrup, S.; Kang, S.; Ly, T.T.; Kim, S.; Choi, Y.H.; Jozwiak, C.; Bostwick, A.; Rotenberg, E.; Park, J.-G.; Sankar, R.; Kim, K.-S.; Kim, J.; Chang, Y.J. Emergence of a Metal−Insulator Transition and High-Temperature Charge-Density Waves in VSe_2 at the Monolayer Limit. *Nano Lett.* **2018**, *18*, 5432−5438.

[9] Coelho, P.M.; Lasek, K.; Cong, K.N.; Li, J.; Niu, W.; Liu, W.; Oleynik, I.I.; Batzill, M. Monolayer Modification of VTe_2 and Its Charge Density Wave. *J. Phys. Chem. Lett.* **2019**, *10*, 4987-4993.

[10] Ugeda, M.M.; Bradley, A.J.; Zhang, Y.; Onishi, S.; Chen, Y.; Ruan, W.; Ojeda Aristizabal, C.; Ryu, H.; Edmonds, M.T.; Tsai, H.-Z.; Riss, A.; Mo, S.-K.; Lee, D.; Zettl, A.; Hussain, Z.; Shen, Z.-X.; Crommie, M.F. Characterization of Collective Ground States in Single-Layer $NbSe_2$. *Nat. Phys.* **2016**, *12*, 92-97.

[11] Xi, X.; Zhao, L.; Wang, Z.; Berger, H.; Forró, L.; Shan, J.; Mak, K.F. Strongly Enhanced Charge-Density-Wave Order in Monolayer $NbSe_2$. *Nat. Nanotechnol.* **2015**, *10*, 765–769.

[12] Chen, Y.; Ruan, W.; Wu, M.; Tang, S.; Ryu, H.; Tsai, H.-Z.; Lee, R., Kahn, S.; Liou, F.; Jia, C.; Albertini, O.R.; Xiong, H.; Jia, T.; Liu, Z.; Sobota, J.A.; Liu, A.Y.; Moore, J.E.; Shen; Z.-X., Louie, S.G.; Mo, S.-K., Crommie, M.F. Strong Correlations and Orbital Texture in Single-Layer 1T-$TaSe_2$. *Nat. Phys.* 2020, *16*, 218–224.

[13] Ciarrocchi, A.; Avsar, A.; Ovchinnikov D.; Kis, A. Thickness-Modulated Metal-to-Semiconductor Transformation in a Transition Metal Dichalcogenide. *Nat. Commun.* **2018**, *9*, 919.

---

[14] Villaos, R.A.B.; Crisostomo, C.P.; Huang, Z.-Q.; Huang, S.-M.; Padama, A.A.B.; Albao, M.A.; Lin, H.; Chuang F.-C. Thickness Dependent Electronic Properties of Pt Dichalcogenides. *npj 2D Mater. Appl.* **2019**, *3*, 2.

[15] Zhao, Y.; Qiao, J.; Yu, P.; Hu, Z.; Lin, Z.; Lau, S.P.; Liu, Z.; Ji, W.; Chai; Y. Extraordinarily Strong Interlayer Interaction in 2D Layered PtS_2. *Adv. Mater.* **2016**, *28*, 2399–2407.

[16] Zhao, Y.; Qiao, J.; Yu, Z.; Yu, P.; Xu, K.; Lau, S.P.; Zhou, W.; Liu, Z.; Wang, X.; Ji, W.; Chai, Y. High-Electron-Mobility and Air-Stable 2D Layered $PtSe_2$ FETs. *Adv. Mater.* **2017**, *29*, 1604230.

[17] Ansari, L.; Monaghan, S.; McEvoy, N.; Coileáin, C.Ó.; Cullen, C.P.; Lin, J.; Siris, R.; Stimpel-Lindner, T.; Burke, K.F.; Mirabelli, G.; Duffy, R.; Caruso, E.; Nagle, R.E.; Duesberg, G.S.; Hurley, P.K.; Gity, F. Quantum Confinement-Induced Semimetal-to-Semiconductor Evolution in Large-Area Ultra-Thin $PtSe_2$ Films Grown at 400°C. *npj 2D Mater. Appl.* **2019**, *3*, 1–8.

[18] Clark, O.J.; Mazzola, F.; Feng, J.; Sunko, V.; Markovic, I.; Bawden, L.; Kim, T.K.; King, P.D.C.; Bahramy, M.S. Dual Quantum Confinement and Anisotropic Spin Splitting in the Multivalley Semimetal $PtSe_2$. *Phys. Rev. B* **2019**, *99*, 045438.

[19] Yan, M.; Huang, H.; Zhang, K.; Wang, E.; Yao, W.; Deng, K.; Wan, G.; Zhang, H.; Arita, M.; Yang, H.; Sun, Z.; Yao, H.; Wu, Y.; Fan, S.; Duan, W.; Zhou. S. Lorentz-Violating Type-II Dirac Fermions in Transition Metal Dichalcogenide $PtTe_2$. *Nat. Commun.* **2017**, *8,* 257.

[20] Huang, H.; Zhou, S.; Duan, W. Type-II Dirac Fermions in the $PtSe_2$ Class of Transition Metal Dichalcogenides. *Phys. Rev. B* **2016**, *94*, 121117(R).

[21] Zhang, K.; Yan, M.; Zhang, H.; Huang, H.; Arita, M.; Sun, Z.; Duan, W.; Wu, Y.; Zhou, S. Experimental Evidence for Type-II Dirac Semimetal in $PtSe_2$. *Phys. Rev. B* **2017**, *96*, 125102.

[22] Yang, H.; Schmidt, M.; Süss, V.; Chan, M.; Balakirev, F.F.; McDonald, R.D.; Parkin, S.S.P.; Felser, C.; Yan, B.; Mol, P.J.W. Quantum Oscillations in the Type-II Dirac Semi-Metal Candidate $PtSe_2$. *New J. Phys.* **2018**, *20*, 043008.

[23] Avsar, A.; Ciarrocchi, A.; Pizzochero, M.; Unuchek, D.; Yazyev, O.V.; Kis, A. Defect Induced, Layer-Modulated Magnetism in Ultrathin Metallic $PtSe_2$. *Nat. Nanotechnol.* **2019**, 14, 674–678.

[24] Avsar, A.; Cheon, C.-Y.; Pizzochero, M.; Tripathi, M.; Ciarrocchi, A.; Yazyev, O.Y.; Kis, A. Probing Magnetism in Atomically Thin Semiconducting $PtSe_2$. *Nat. Commun.* **2020**, *11*, 4806.

[25] Lin, M.-K.; Villaos, R.A.B.; Hlevyack, J.A.; Chen, P.; Liu, R.-Y.; Hsu, C.-H.; Avila, J.; Mo, S.-K.; Chuang, F.-C.; Chiang. T.C. Dimensionality-Mediated Semimetal-Semiconductor Transition in Ultrathin $PtTe_2$ Films. *Phys. Rev. Lett.* **2020**, *124*, 036402

[26] Yao, W.; Wang, E.; Huang, H.; Deng, K.; Yan, M.; Zhang, K.; Miyamoto, K.; Okuda, T.; Li, L.; Wang, Y.; Gao, H.; Liu, C.; Duan, W.; Zhou, S. Direct Observation of Spin-Layer Locking by Local Rashba Effect in Monolayer Semiconducting $PtSe_2$ Film. *Nat. Commun.* **2017**, *8*, 14216.

[27] Yan, M.; Wang, E.; Zhou, X.; Zhang,G.; Zhang, H.; Zhang, K.; Yao, W.; Lu, N.; Yang, S.; Wu, S.; Yoshikawa, T.; Miyamoto, K.; Okuda, T.; Wu, Y.; Yu, P.; Duan, W.; Zhou, S. High Quality Atomically Thin $PtSe_2$ Films Grown by Molecular Beam Epitaxy. *2D Mater.* **2017**, *4*, 045015.

---

[28] Wang, Z.; Li, Q.; Besenbacher, F.; Dong, M. Facile Synthesis of Single Crystal $PtSe_2$ Nanosheets for Nanoscale Electronics. *Adv. Mater.* **2016**, *28*, 10224-10229.

[29] Lin, X.; Lu, J.C.; Shao, Y.; Zhang, Y.Y.; Wu, X.; Pan, J.B.; Gao, L.; Zhu, S.Y.; Qian, K.; Zhang, Y.F.; Bao, D.L.; Li, L.F.; Wang, Y.Q.; Liu, Z.L.; Sun, J.T.; Lei, T.; Liu, C.; Wang, J.O.; Ibrahim, K.; Leonard, D.N.; Zhou, W.; Guo, H,M.; Wang, Y.L.; Du, S.X.; Pantelides, S.T.; Gao H.-J. Intrinsically Patterned Two-Dimensional Materials for Selective Adsorption of Molecules and Nanoclusters. *Nat. Mater.* 2017, *16*, 717–721.

[30] Kempt, R.; Kuc, A.; Heine. T. Two-Dimensional Noble-Metal Chalcogenides and Phosphochalcogenides. *Angew. Chem. Int. Ed.* **2020**, *59*, 9242-9254.

[31] Zhang, K.; Wang, M.; Zhou, X.; Wang, Y.; Shen, S.; Deng, K.; Peng, H.; Li, J.; Lai, X.; Zhang, L.; Wu, Y.; Duan, W.; Yu, P.; Zhou, S. Growth of Large Scale PtTe, $PtTe_2$ and $PtSe_2$ Films on a Wide Range of Substrates. *Nano Res.* **2021**, *14*, 1663–1667.

[32] Yan, M.; Wang, E.; Zhou, X.; Zhang, G.; Zhang, H.; Zhang, K.; Yao, W.; Lu, N.; Yang, S.; Wu, S.; Yoshikawa, T.; Miyamoto, K.; Okuda, T.; Wu, Y.; Yu, P.; Duan, W.; Zhou, S. High Quality Atomically Thin $PtSe_2$ Films Grown by Molecular Beam Epitaxy. *2D Mater.* **2017**, *4*, 045015.

[33] Politano, A., Chiarello, G., Kuo, C.-N., Lue, C. S., Edla, R., Torelli, P., Pellegrini, V., Boukhvalov, D. W., Tailoring the Surface Chemical Reactivity of Transition-Metal Dichalcogenide $PtTe_2$ Crystals. *Adv. Funct. Mater.* **2018**, *28*, 1706504

[34] Shi, J.; Huan, Y.; Hong, M.; Xu, R.; Yang, P.; Zhang, Z.; Zou, X.; Zhang, Y. Chemical Vapor Deposition Grown Large-Scale Atomically Thin Platinum Diselenide with Semimetal–Semiconductor Transition. *ACS Nano* **2019**, *13*, 8442-8451.

[35] Zhou, J.; Kong, X.; Sekhar, M.C.; Lin, J.; Le Goualher, F.; Xu, R.; Wang, X.; Chen, Y.; Zhou, Y.; Zhu, C.; Lu, W.; Liu, F.; Tang, B.; Guo, Z.; Zhu, C.; Cheng, Z.; Yu, T.; Suenaga, K.; Sun, D.; Ji, W.; Liu, Z. Epitaxial Synthesis of Monolayer $PtSe_2$ Single Crystal on $MoSe_2$ with Strong Interlayer Coupling. *ACS Nano* **2019**, *13*, 10929-10938.

[36] Wang, Y.; Li, L.; Yao, W.; Song, S.; Sun, J.T.; Pan, J.; Ren, X.; Li, C.; Okunishi, E.; Wang, Y.-Q.; Wang, E.; Shao, Y.; Zhang, Y.Y.; Yang, H.T.; Schwier, E.F.; Iwasawa, H.; Shimada, K.; Taniguchi, M.; Cheng, Z.; Zhou, S.; Du, S.; Pennycook, S.J.; Pantelides, S.T.; Gao, H.-J. Monolayer $PtSe_2$, a New Semiconducting Transition-Metal Dichalcogenide, Epitaxially Grown by Direct Selenization of Pt. *Nano Lett.* **2015**, *15*, 4013−4018*.*

[37] Miró, P.; Ghorbani-Asl, M.; Heine, T. Two Dimensional Materials beyond MoS_2: Noble-Transition-Metal Dichalcogenides. *Angew. Chem. Int. Ed.* **2014**, *53*, 3015-3018.

[38] Ugeda, M.M.; Bradley, A.J.; Shi, S-F.; da Jornada, F.H.; Zhang, Y.; Qiu, D.Y.; Ruan, W.; Mo, S.-K.; Hussain, Z.; Shen, Z.-X.; Wang, F.; Louie, S.G.; Crommie, M.F. Giant Bandgap Renormalization and Excitonic Effects in a Monolayer Transition Metal Dichalcogenide Semiconductor. *Nat. Mater.* **2014**, *13*, 1091–1095.

[39] Bruix, A.; Miwa, J.A.; Hauptmann, N.; Wegner, D.; Ulstrup, S.; Grønborg, S.S.; Sanders, C.E.; Dendzik, M.; Čabo, A.G.; Bianchi, M.; Lauritsen, J.V.; Khajetoorians, A. A.; Hammer, B.;

Hofmann, P. Single-Layer MoS$_2$ on Au(111): Band Gap Renormalization and Substrate Interaction. *Phys. Rev. B* **2016**, *93*, 165422.

[40] Zhang, C.; Johnson, A.; Hsu, C.L.; Li, L.-J.; Shih, C.-K. Direct Imaging of Band Profile in Single Layer MoS$_2$ on Graphite: Quasiparticle Energy Gap, Metallic Edge States, and Edge Band Bending. Nano Lett. **2014**, *14*, 2443–2447.

[41] Huang, Y.L.; Chen, Y.; Zhang, W.; Quek, S.Y.; Chen, C.-H.; Li, L.-J.; Hsu, W.-T.; Chang, W.-H.; Zheng, Y.Z.; Chen, W.; Wee, A.T.S. Bandgap Tunability at Single-Layer Molybdenum Disulphide Grain Boundaries. *Nat. Commun.* **2015**, *6*, 6298.

[42] Murray, C.; Jolie, W.; Fischer, J.A.; Hall, J.; van Efferen, C.; Ehlen, N.; Grüneis, A.; Busse, C.; Michely, T. Comprehensive Tunneling Spectroscopy of Quasi-Freestanding MoS$_2$ on Graphene on Ir(111). *Phys. Rev. B* **2019**, *99*, 115434

[43] Shi, H.; Pan, H.; Zhang, Y.-W.; Yakobson, B.I. Quasiparticle Band Structures and Optical Properties of Strained Monolayer MoS$_2$ and WS$_2$ *Phys. Rev. B* **2013**, *87*, 155304.

[44] Qiu, D.Y.; da Jornada, F.H.; Louie, S.G. Optical Spectrum of MoS$_2$: Many-Body Effects and Diversity of Exciton States. *Phys. Rev. Lett.* **2015**, *111*, 216805.

[45] Rasmussen, F.A.; Schmidt, P.S.; Winther, K.T.; Thygesen, K.S. Efficient Many-Body Calculations for Two-Dimensional Materials Using Exact Limits for the Screened Potential: Band Gaps of MoS$_2$, H-BN, and Phosphorene. *Phys. Rev. B* **2016**, *94*, 155406.

[46] Shawkat, M.S.; Gil, J.; Han, S.S; Ko, T.-J.; Wang, M.; Dev, D.; Kwon, J.; Lee, G.-H.; Oh, K.H.; Chung, H.-S.; Roy, T.; Jung, Y.J.; Jung, Y. Thickness-Independent Semiconducting-to-Metallic Conversion in Wafer-Scale Two-Dimensional PtSe$_2$ Layers by Plasma-Driven Chalcogen Defect Engineering. *ACS Appl. Mater. Interf.* **2020**, *12*, 14341–14351.

[47] Grønvold, F.; Haraldsen, H.; Kjekshus, A. On the Sulfides, Selenides, and Tellurides of Platinum. *Acta Chem. Scandinavia* **1960**, *14*, 1879-1893.

[48] Zhao, Z.; Zhang, H.; Yuan, H.; Wang, S.; Lin, Y.; Zeng, Q.; Xu, G.; Liu, Z.; Solanki, G.K.; Patel, K.D.; Cui, Y.; Hwang, H.Y.; Mao, W.L. Pressure Induced Metallization with Absence of Structural Transition in Layered Molybdenum Diselenide. *Nat. Commun.* **2015**, *6*, 7312.

[49] Kresse, G.; Hafner, J. *Ab Initio* Molecular Dynamics for Liquid Metals. *Phys. Rev. B* **1993**, *47*, *558(R).*

[50] Perdew, J.P.; Burke, K.; Ernzerhof, M. Generalized Gradient Approximation Made Simple. *Phys. Rev. Lett.* **1996**, *77*, 3865.

[51] Grimme, S.; Antony, J.; Ehrlich, S.; Krieg, H. A Consistent and Accurate *ab Initio* Parametrization of Density Functional Dispersion Correction (DFT-D) for the 94 Elements H-Pu. *J. Chem. Phys.* **2010**, *132*, 154104.

[52] Klimeš, J.; Bowler, D.R.; Michaelides, A. Chemical Accuracy for the van der Waals Density Functional. *J. Phys.: Condens. Matter* **2009**, *22*, 022201.

[53] Tawfik, S.A.; Gould, T.; Stampfl, C.; Ford, M.J. Evaluation of van der Waals Density Functionals for Layered Materials. *Phys. Rev. Mater.* **2018**, *2*, 034005.

---

[54] Heyd, J.; Scuseria. G.E. Hybrid Functionals Based on a Screened Coulomb Potential. J*. Chem. Phys.* **2003**, *118*, 8207.

[55] Paier, J.; Marsman, M.; Hummer, K.; Kresse, G.; Gerber, I.C.; Ángyán, J.G. Screened Hybrid Density Functionals Applied to Solids. *J. Chem. Phys.* **2006**, *124*, 154709.

[56] Hedin, L. New Method for Calculating the One-Particle Green's Function with Application to the Electron-Gas Problem. *Phys. Rev.* **1965**, *139*, A796.

[57] Shishkin, M.; Kresse, G. Implementation and Performance of the Frequency-Dependent GW Method within the PAW Framework. *Phys. Rev. B* **2006**, *74*, 035101.